Supplementary Information for

Framework-Templated Gas Lattices in Metal-Organic Frameworks

Younghun Kim[1‡], Dohoon Kim[1‡], Seungwoo Kim[1], Yunsung Lim[1,2], Jihan Kim[1]*

[1]Department of Chemical and Biomolecular Engineering, Korea Advanced Institute of Science and Technology, Daejeon 34141, Republic of Korea

[2]Department of Material Science and Engineering, Seoul National University, Seoul 08826, Republic of Korea

*Corresponding Author: jihankim@kaist.ac.kr (J. K.)

These authors contributed equally: Younghun Kim, Dohoon Kim

This PDF file includes:

Supplementary Fig. 1 to 15

Supplementary Tables 1 to 2

Supplementary Notes 1 to 4

References 1 to 10

Supplementary Information

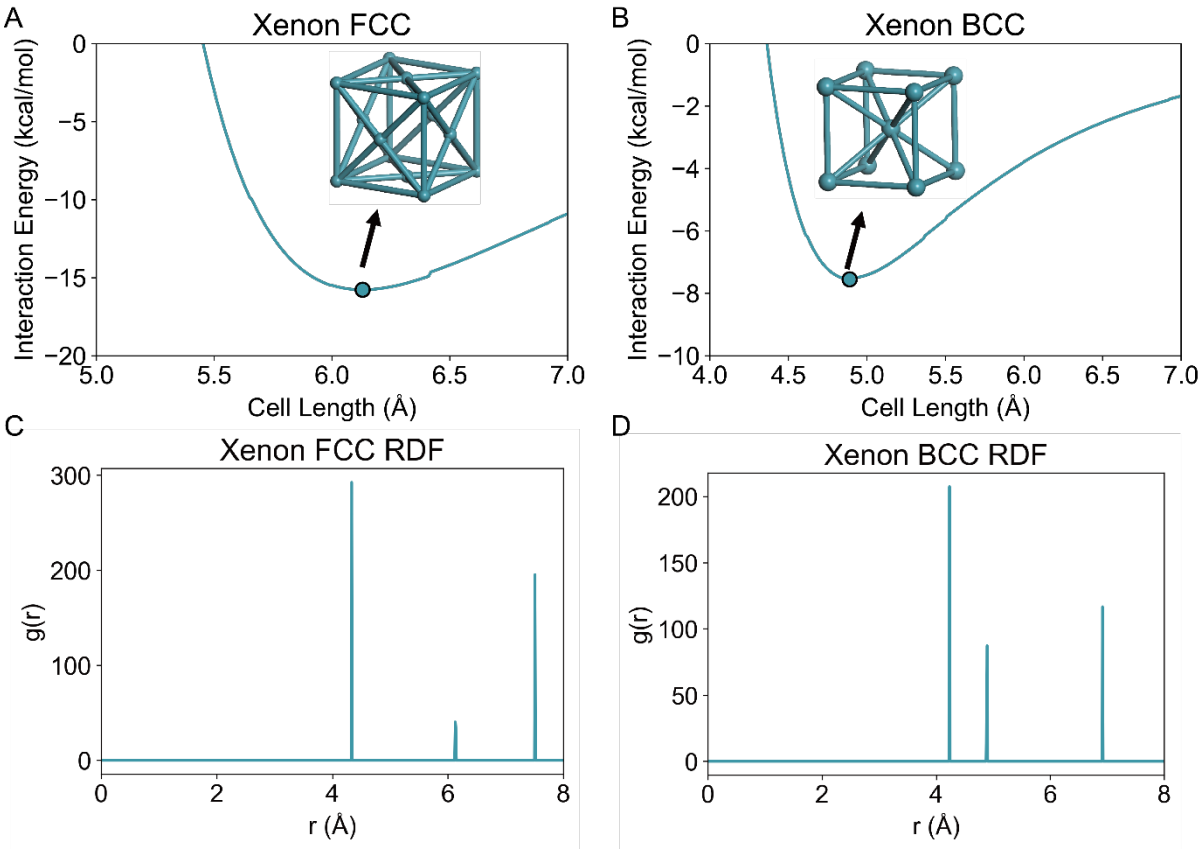

Supplementary Fig. 1: Interaction-energy and RDF references for ideal Xenon FCC and BCC lattices. Top: The lattice constant was systematically varied for each crystal (FCC, left; BCC, right) and the Xenon–Xenon potential energy was evaluated per unit cell to identify the energetically preferred spacing. Markers denote the energy minima and the corresponding representative lattice configurations. The FCC minimum occurs at a lattice constant of 6.13 Å, whereas the BCC minimum occurs at 4.89 Å. Bottom: Corresponding ideal-lattice radial distribution functions (RDFs) used as reference signatures. The FCC RDF shows peaks at 4.34 Å, 6.13 Å, and 7.53 Å, while the BCC RDF shows peaks at 4.23 Å, 4.89 Å, and 6.93 Å.

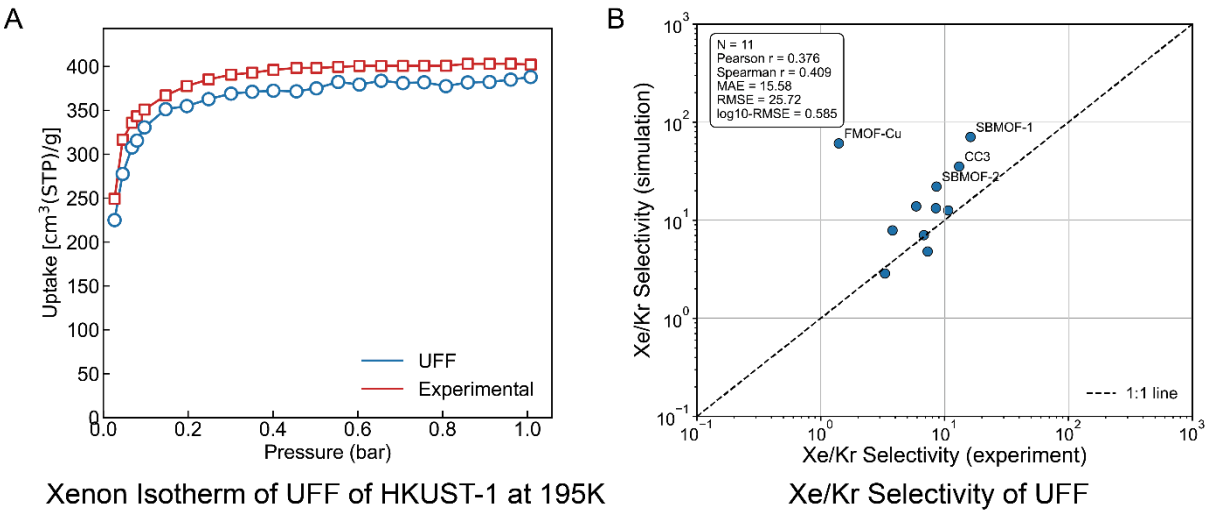

Supplementary Fig. 2: Sanity-check comparison of UFF-based adsorption trends against external experimental data. A) Xenon adsorption isotherm calculated at 195K using UFF compared with an experimentally reported Xenon isotherm taken from the literature[1]. B) Comparison between simulated and experimentally reported Xe/Kr selectivities for a representative set of MOFs. The simulated values were obtained using UFF, while the experimental data were collected from prior literature reports[2]. The dashed line indicates the 1:1 relation. These comparisons support the use of UFF as a screening-level force field that reproduces the overall adsorption and selectivity trends with reasonable fidelity.

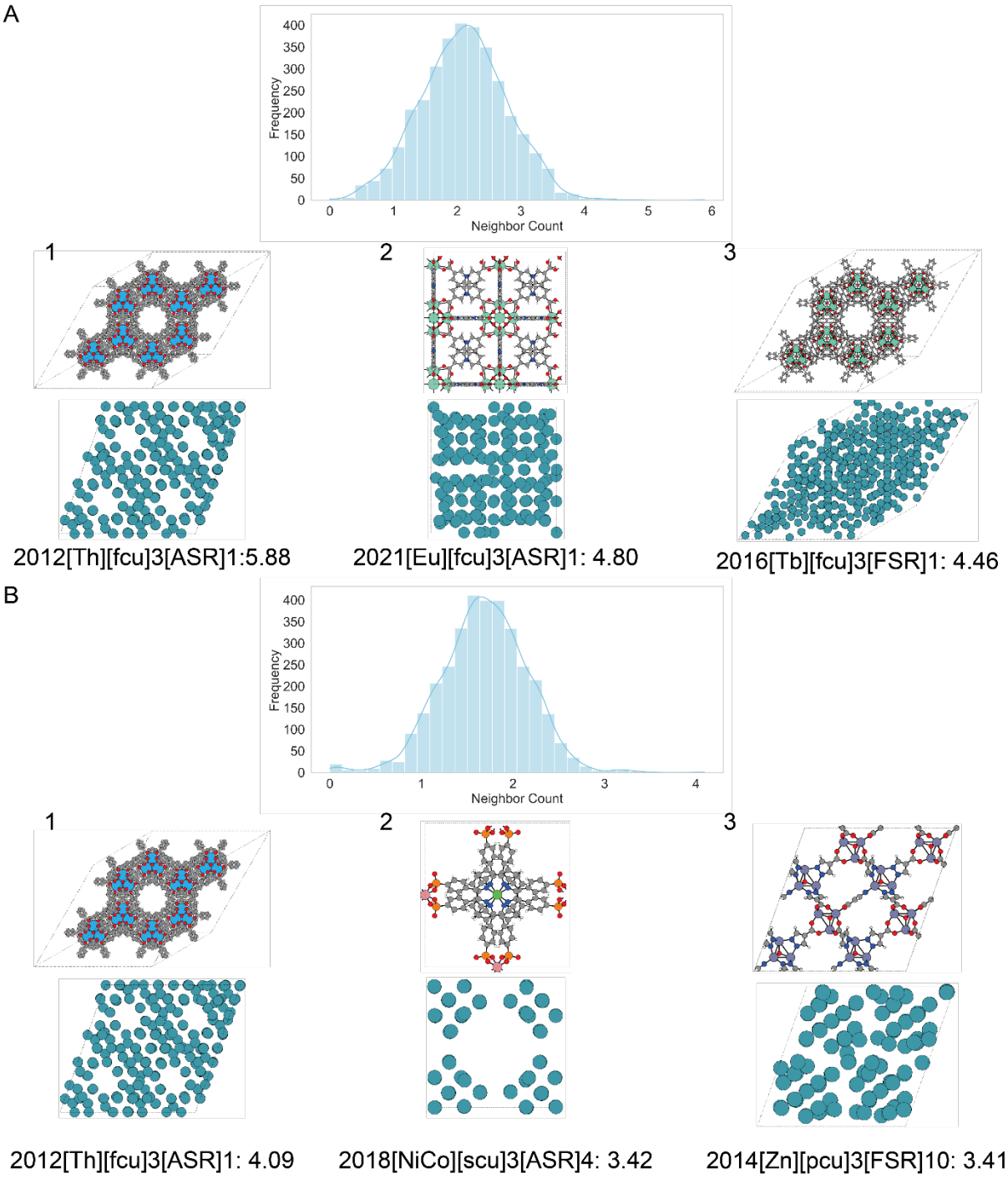

Supplementary Fig. 3: Screening results of gas lattice neighbor counts for FCC and BCC phases. Distribution plot of CoREMOF[3] on A) FCC gas lattice and B) BCC gas lattice with their top 3 neighbor count structure along with their neighbor count scores. The top shows the structure of the corresponding MOFs and the bottom shows the Xenon snapshots.

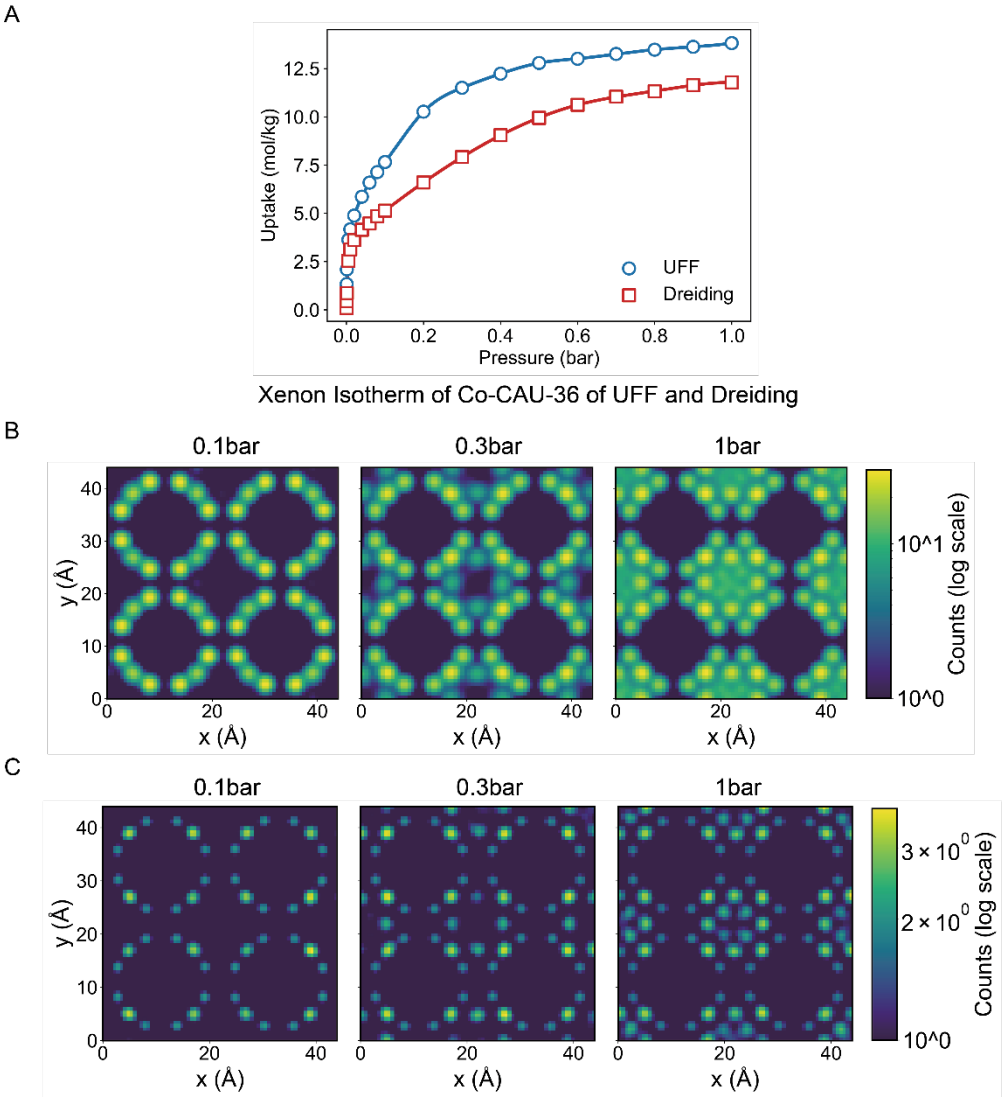

Supplementary Fig. 4: Robustness of Xenon gas-lattice formation with respect to framework force-field choice. A) Xenon adsorption isotherms in Co-CAU-36 calculated using UFF and Dreiding. Although the absolute uptake differs quantitatively between the two force fields, both predict substantial Xenon adsorption over the same pressure range. Ensemble-averaged Xenon density maps in Co-CAU-36 at increasing pressures, calculated using UFF B) and Dreiding C), respectively. In both cases, the same qualitative evolution is observed: initial shell-site occupation, followed by pore filling, and the emergence of an ordered gas-lattice-like arrangement at higher loading. These results indicate that the framework-templated Xenon gas lattice is not an artifact of the UFF description, although quantitative details remain force-field dependent.

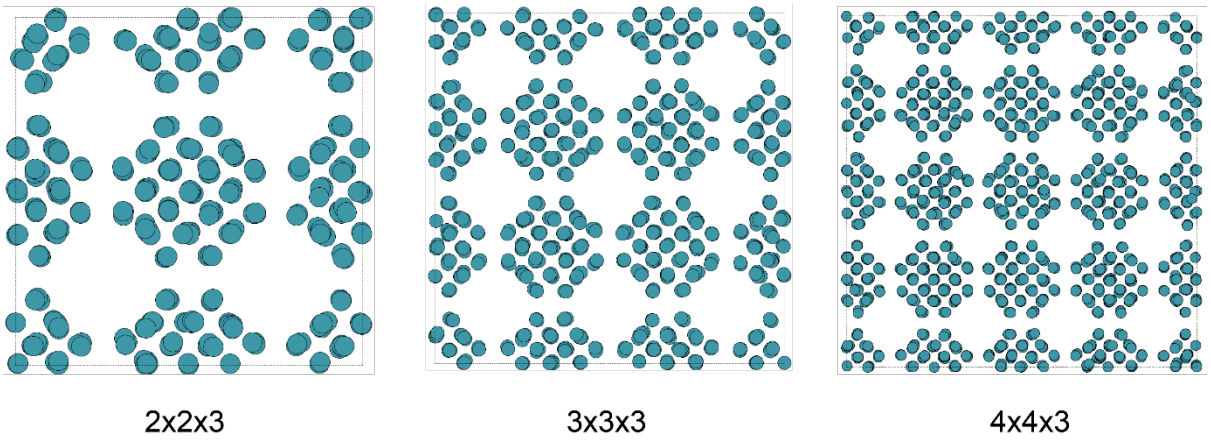

Supplementary Fig. 5: Box-size convergence of the Xenon gas-lattice configuration in Co-CAU-36. Representative Xenon adsorption snapshots obtained from simulations performed with progressively larger supercells. The system size is increased while preserving the same framework topology and adsorption conditions. In all cases, the same qualitative framework-templated ordering is retained, demonstrating that the observed Xenon gas lattice is not a finite-size artifact of the original simulation cell.

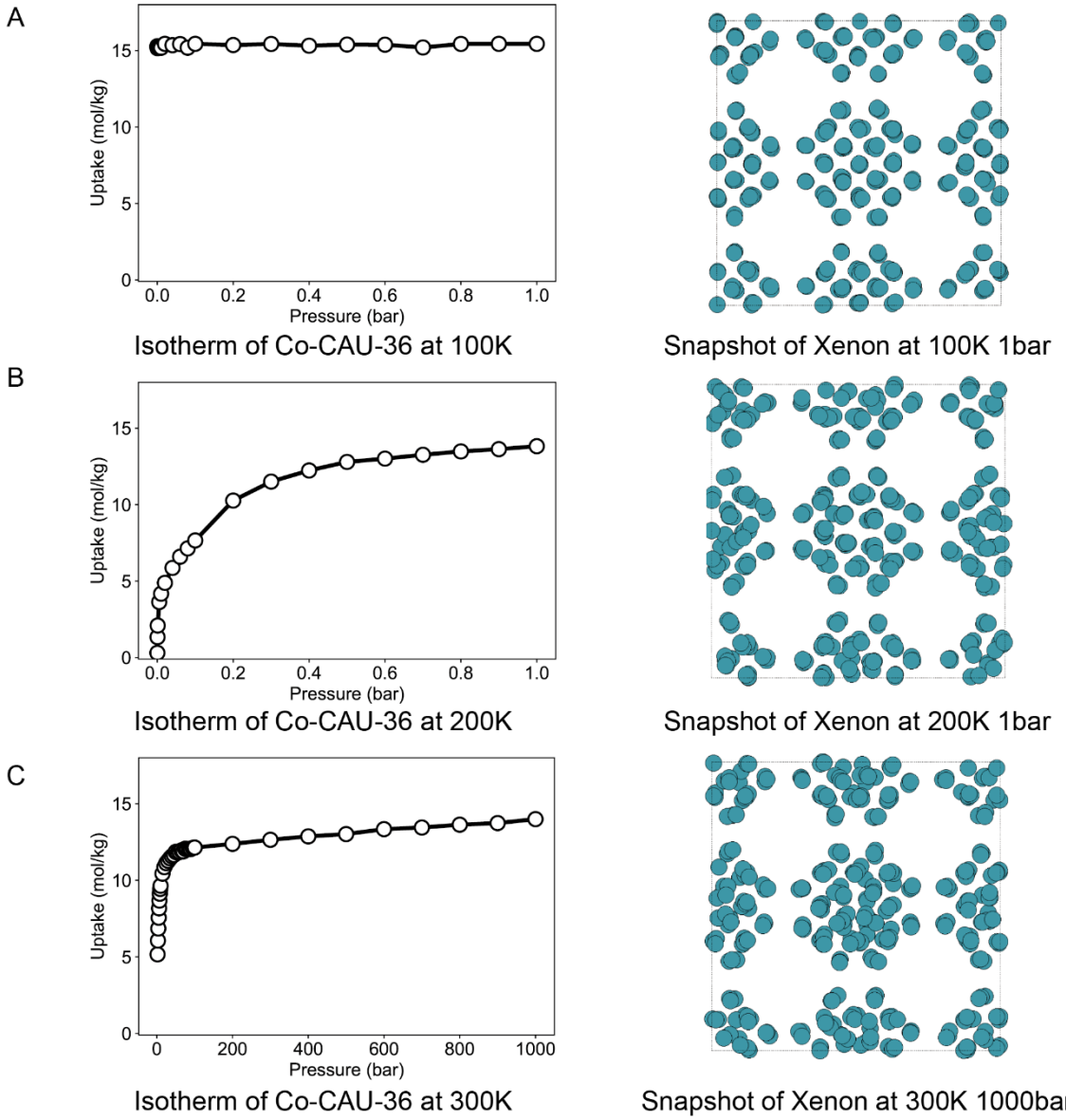

Supplementary Fig. 6: Representative adsorption isotherms of Co-CAU-36. Co-CAU-36[4] isotherm at A) 100K, B) 200K, and C) 300K (left) and corresponding real-space Xenon configurations (right) illustrating distinct adsorption regimes in Co-CAU-36. The 100K snapshot shows near-saturated uptake with a dense, pore-filling arrangement, a pronounced low-pressure uptake with progressive filling toward a high-loading state at 200K, and suppressed low-pressure adsorption with substantial pore filling achieved at very high pressure at 300 K. The 300 K pressure range was extended to 1000 bar to access a Xenon loading comparable to the dense filled states observed at lower temperatures.

Supplementary Note 1. DFT validation of the Xenon gas lattice and adsorption sites in Co-CAU-36.

Additional validation of the robustness of gas lattice was conducted with geometric optimization through Density Functional Theory (DFT) calculations. DFT calculations were carried out using the Vienna Ab initio Simulation Package (VASP)[5]. Co-CAU-36 was first geometry-optimized, after which a Xenon gas lattice was positioned using GCMC snapshots, and the combined MOF+Xe system was optimized again to confirm the stability and feasibility of the gas lattice at a higher level of theory.

Exchange–correlation interactions were described using the generalized gradient approximation (GGA) with the PBE functional. The PAW method was used for electron–ion interactions (ref), with a plane-wave kinetic energy cutoff of 520 eV. Long-range dispersion interactions were included via DFT-D3 (Grimme) corrections[6]. Spin polarization was enabled to capture potential magnetic effects in the MOF when relevant. Electronic partial occupancies were treated with Gaussian smearing (0.05 eV). Structural relaxations were performed without symmetry constraints, relaxing both atomic positions and lattice parameters. Convergence thresholds were set to 10^{-5}eV for electronic self-consistency and 0.01 eV/Å for ionic relaxation.

For comparison with the force-field adsorption landscape, UFF-based interaction-energy grids were generated and local minima were identified using a 1.0 Å cutoff criterion. Each DFT-optimized Xenon site was then matched to the nearest UFF grid minimum. The agreement between the DFT and force-field descriptions was quantified by averaging the interaction-energy differences and site-to-site distances between the matched adsorption sites.

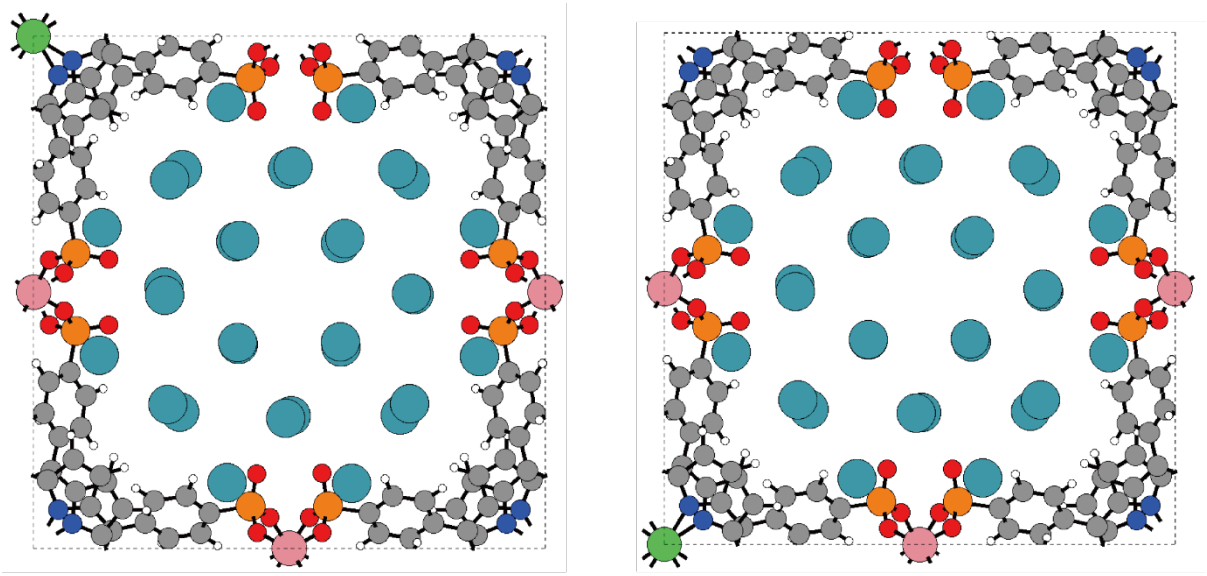

Supplementary Fig. 7: DFT level robustness of Xenon gas lattice in Co-CAU-36. The ordered configuration of the gas lattice remained stable after geometric optimization.

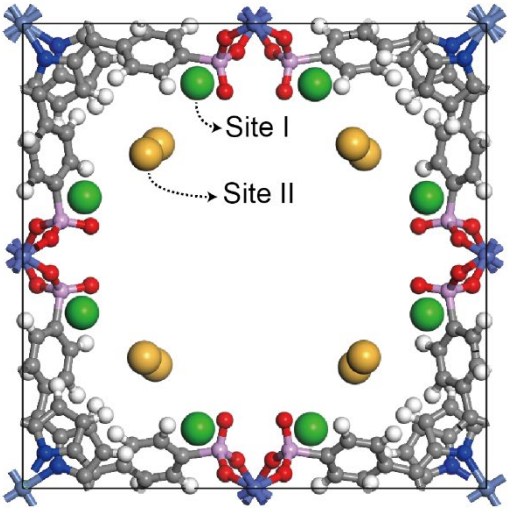

Supplementary Fig. 8: Consistency of Xenon adsorption shell sites between DFT and force-field calculations in Co-CAU-36. Interaction energies and site-to-site distances confirm the consistency of the Xenon adsorption sites across the two levels of theory.

	$E_{int,DFT}$ (kcal/mol)	$E_{int,FF}$ (kcal/mol)	DFT–FF Site Distance (Å)
Site I	-7.46±0.14	-7.21±0.00	0.12±0.03
Site II	-4.56±0.05	-4.34±0.00	0.61±0.13

Supplementary Table 1. Comparison of Xenon adsorption sites between DFT and force-field calculations. Mean interaction energies and mean DFT–FF site distances are summarized for the representative sites identified in Co-CAU-36.

Supplementary Note 2. Flexibility Analysis of Co-CAU-36 with Melt-Quenching Simulation

Flexibility analysis of Co-CAU-36 was conducted using classical Molecular Dynamics simulation (MD). Classical MD simulations were conducted using Large-scale Atomic/Molecular Massively Parallel Simulator (LAMMPS)[7]. UFF forcefield[8] was used for the MOF and reported parameters for the Xenon was used[2]. MD was used in two distinct contexts. First, to test the robustness and reversibility of gas lattice of Xenon, we performed a melt–quench thermal perturbation protocol under the NVT ensemble, using a fixed Xenon loading (i.e., not intended to represent equilibrium adsorption amounts at each temperature). Specifically, we simulated 5 ns at 500 K, followed by 5 ns at 300 K, and 5 ns at 100 K, and monitored whether the Xenon configuration recovered its gas lattice during cooling.

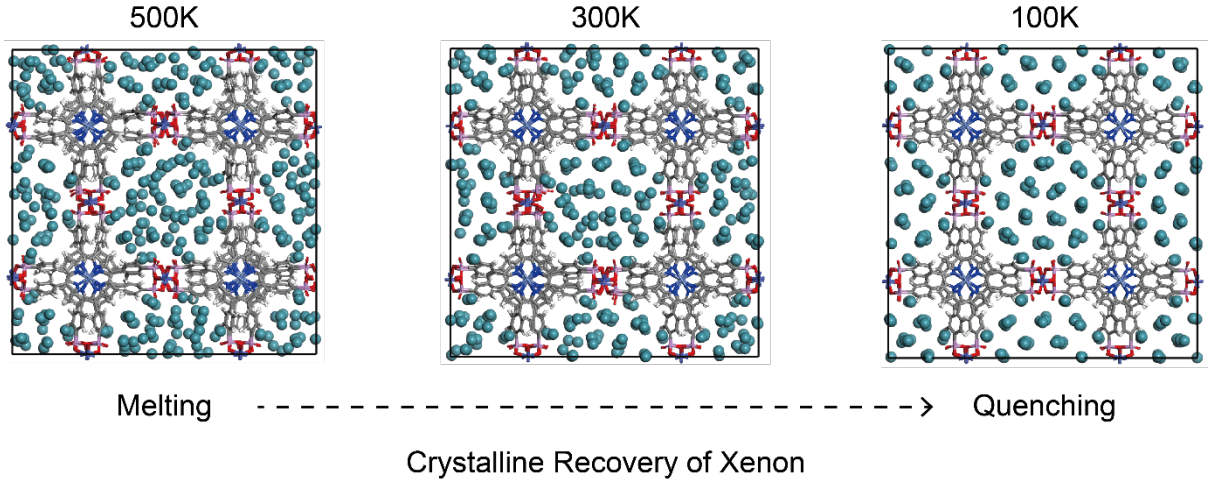

Supplementary Fig. 9: Snapshots of the Melt-Quenching simulation conducted on Co-CAU-36. From left to right are the snapshot of Xenon at 500K, 300K and 100K. The degree of ordering increases as snapshot quenches.

	ε/k (K)	σ(Å)
Argon[9]	115.0	3.41
Krypton[2]	165.2	3.66
Methane[10]	148.0	3.73
Xenon[2]	229.8	3.97

Supplementary Table 2. Force field parameters for one-body guest atoms.

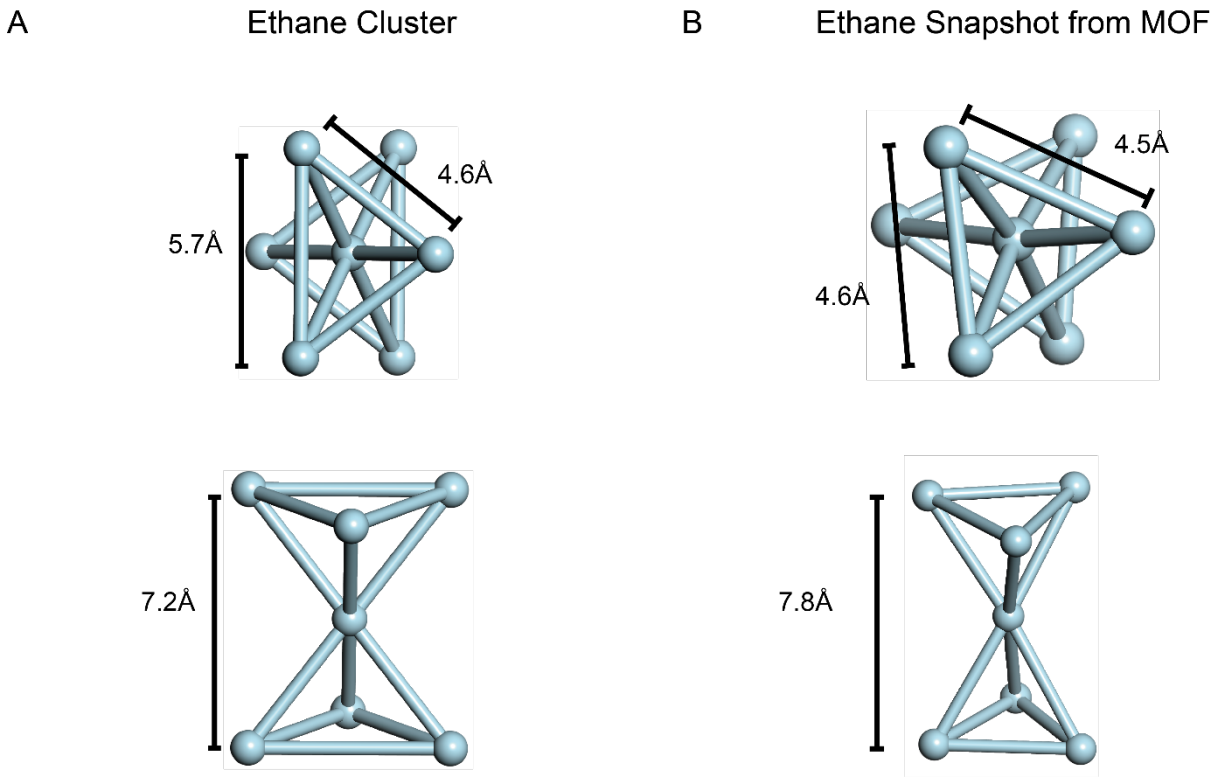

Supplementary Fig. 10: Distance and cluster comparison between the reference ethane lattice and the confined ethane motif in the MOF. Comparison of the A) local COM geometry of the reference BCC ethane lattice and B) the ordered ethane cluster extracted from the MOF snapshot.

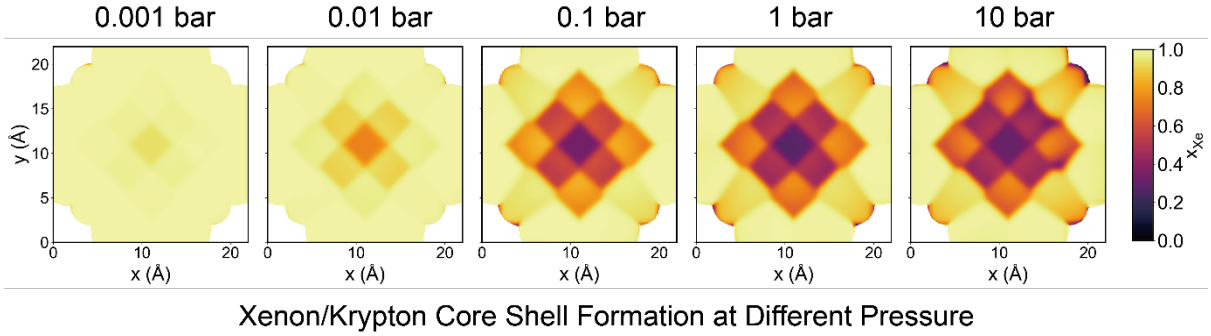

Supplementary Fig. 11: Xenon/Krypton co-adsorption of Co-CAU-36 of different pressure region at 100K. From left to right: 0.001 bar, 0.01 bar, 0.1 bar, 1 bar, and 10 bar. Similar pore scale partitioning is noticed for all pressure range.

Supplementary Note 3. Nudged Elastic Band Calculation

Nudged Elastic Band (NEB) calculations were performed using the LAMMPS package[7] to determine the minimum energy pathway between the initial and final states. The force field parameters for the metal–organic framework (MOF) were assigned using the UFF[8]. Nonbonded interactions were modeled using a Lennard–Jones (LJ) potential with a cutoff distance of 12.5 Å.

During the NEB calculations, the MOF framework atoms were kept fixed, while the Xenon and Krypton gas atoms were allowed to fully relax. Prior to the NEB calculations, the system was energy-minimized using the FIRE algorithm with a maximum atomic displacement of 0.05 Å. The NEB method was applied with a spring constant of 10.0 kcal/mol/Å^2 to couple adjacent images. Twelve intermediate images were placed between the initial and final states. The convergence criteria were set to an energy tolerance and a force tolerance of 1.0×10^{-5}.

NEB was conducted on a partial lattice pathway from the 100K GCMC snapshot. We selected two NEB diffusion pathways to match the distinct transport environments created by shell–core segregation: Krypton migrating between shell sites, and Krypton migrating along the channel core. These sites were chosen because Xenon primarily occupies the strongly templated shell near binding sites and because co-adsorption with Xenon redistributes Krypton into the more open core, where long-axis transport is expected to be least hindered. These two scenarios isolate the effects of species identity and spatial pathway on the migration barrier, directly linking adsorption-driven partitioning to the emergence of a low-resistance diffusion corridor for Krypton.

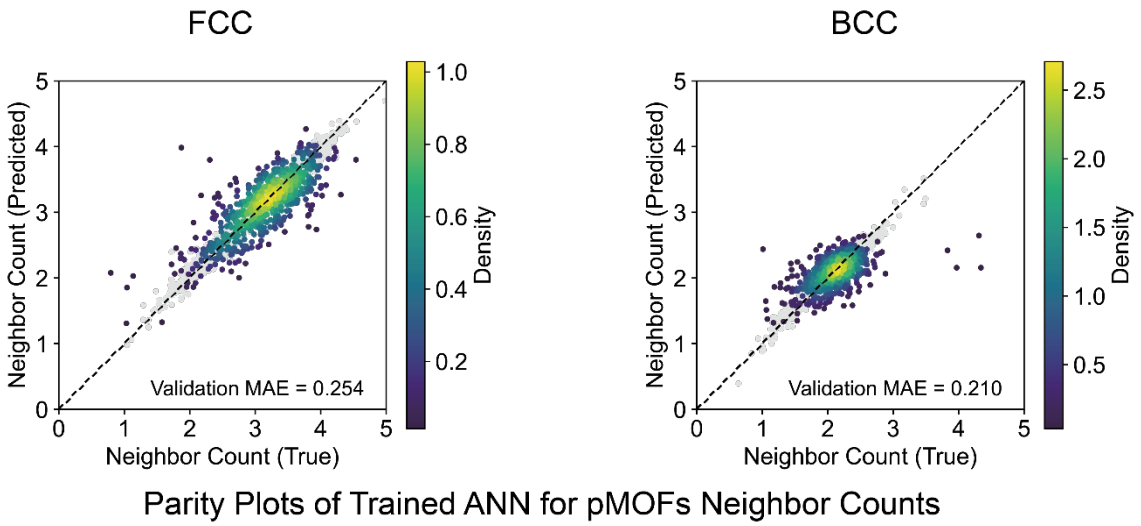

Supplementary Fig. 12: Parity plots of sql FCC and BCC lattice. Parity plots evaluating the machine-learning surrogate models trained to predict the neighbor-count gas lattice descriptor for sql pMOFs targeting FCC (left) and BCC (right) lattice objectives. Predicted versus GCMC-calculated neighbor counts are shown for the validation set (n = 600). The dashed line indicates ideal parity, and the point color reflects data density. The grey points represent the trained set and the gaussian plot shows the validations set. Model performance metrics are reported as mean absolute error (MAE) in each panel.

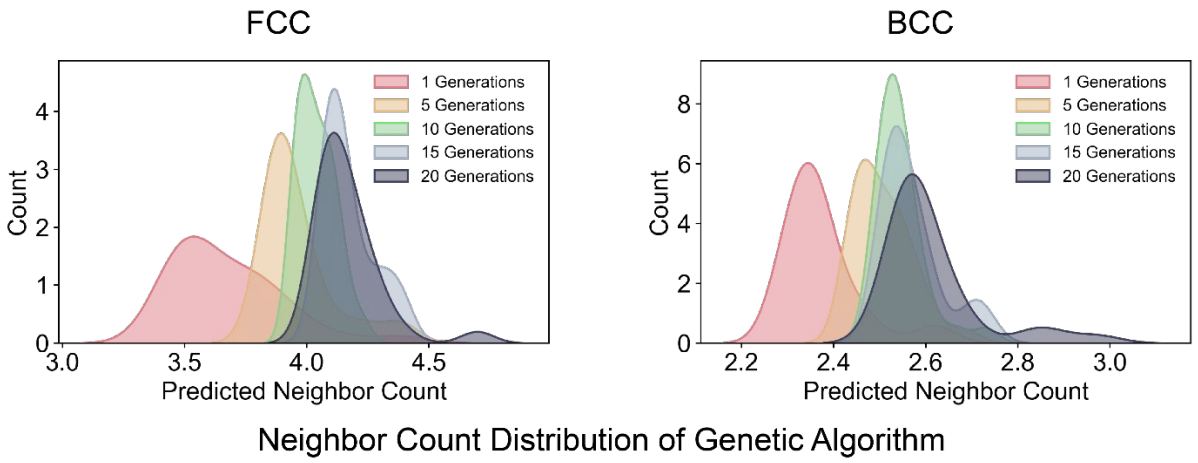

Supplementary Fig. 13: Neighbor count distribution of Genetic Algorithm of FCC and BCC lattice. Evolution of the predicted neighbor-count distributions over genetic-algorithm generations for pMOF inverse design for FCC(left) and BCC(right) lattice. Kernel-density estimates show a progressive right-shift of the population from the initial random generation to later generations (1, 5, 10, 15, 20), indicating enrichment of candidates with higher predicted neighbor counts.

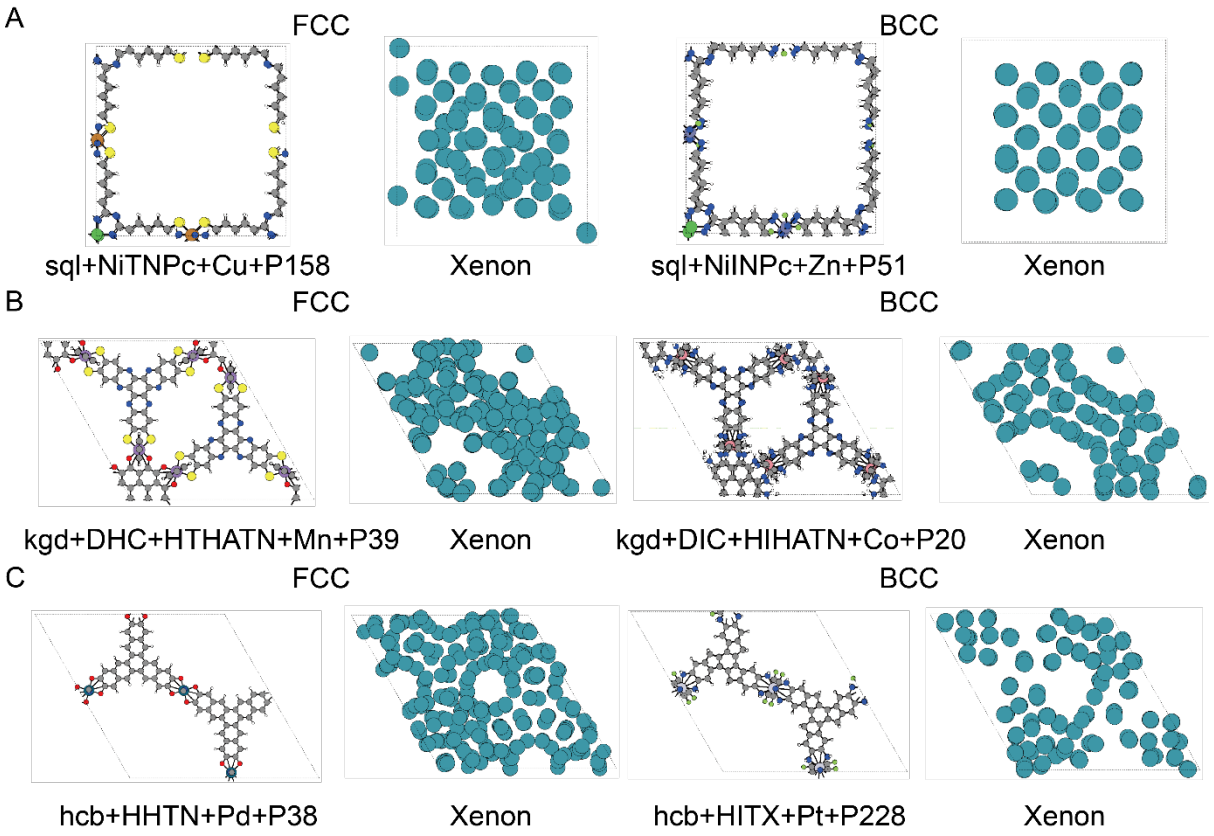

Supplementary Fig. 14: Top GA candidates across pMOF topologies after explicit GCMC validation. Shown are the highest-scoring genetic-algorithm (GA) structures (based on GCMC-derived neighbor counts) for FCC- and BCC-targeted searches in A) sql, B) hcb, and C) kgd pMOF families. For each candidate, the corresponding Xenon adsorption snapshot from the validation simulation is shown on the right. The hxl family is not included because too few viable hxl-based pMOF candidates were generated to support a meaningful GA selection and comparison. Notably, among the topologies evaluated, only sql-based pMOFs exhibited clear, extended framework-templated Xenon ordering consistent with a gas-lattice motif, whereas hcb and kgd candidates remained comparatively disordered under the same validation conditions.

Supplementary Note 4. Top pMOFs candidates

The BCC-targeted winner, sql+NiINPc+Zn+P51, uses an imino- and Ni-functionalized NPc layer coordinated by Zn nodes and pillared by P51 (N_2F_4, tetrafluorohydrazine). The FCC-targeted candidate, sql+NiTNPc+Cu+P158, uses a thiol- and Ni-functionalized NPc layer coordinated by Cu nodes and pillared by P158 (HN_5-NH_2, aminopentazole).

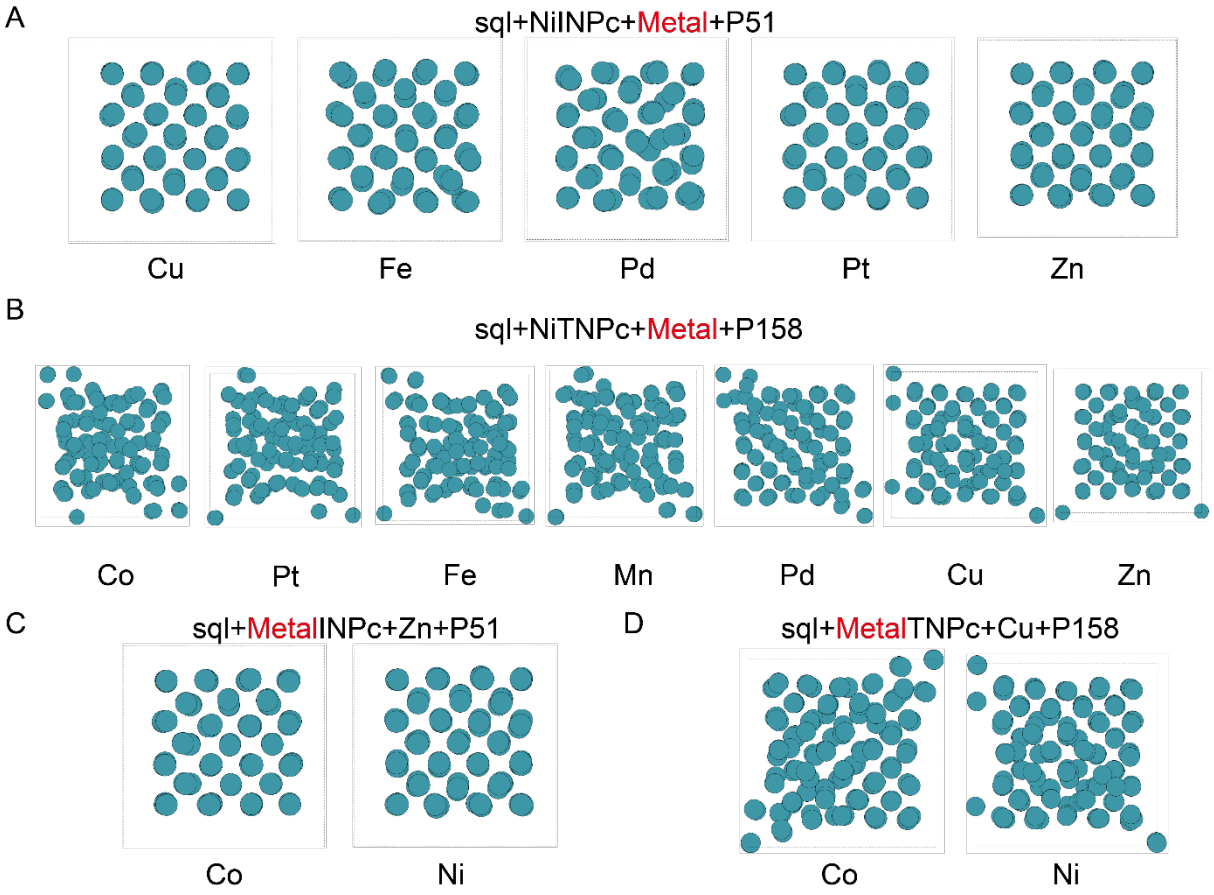

Supplementary Fig. 15: Metal-substitution sensitivity of inverse-designed pMOF gas-lattice candidates. Effect of substituting the 2D-layer metal nodes in the BCC-targeted (A) and FCC-targeted (B) pMOF candidates, shown as representative Xenon configurations at identical conditions. The BCC candidate retains a comparatively consistent lattice-like arrangement across substitutions, whereas the FCC candidate exhibits larger configuration variability and more frequent loss of registry, indicating stronger dependence on the 2D-layer metal for stabilizing the FCC-type lattice. Effect of substituting the central metal in the NPc macrocycle for the BCC-targeted (C) and FCC-targeted (D) candidates. Compared to 2D-layer metal substitution, changing the NPc-centered metal produces smaller qualitative changes in the observed Xenon ordering trends, supporting that lattice stabilization is primarily governed by the 2D-layer + pillar-defined channel geometry and its periodic binding template.

References

1 Elsaidi, S. K. *et al.* Metal organic frameworks for xenon storage applications. *ACS Materials Letters* **2**, 233-238 (2020).

2 Lim, Y., Park, J., Lee, S. & Kim, J. Finely tuned inverse design of metal–organic frameworks with user-desired Xe/Kr selectivity. *Journal of Materials Chemistry A* **9**, 21175-21183 (2021).

3 Zhao, G. *et al.* CoRE MOF DB: A curated experimental metal-organic framework database with machine-learned properties for integrated material-process screening. *Matter* **8** (2025).

4 Wang, B. *et al.* A Porous Cobalt Tetraphosphonate Metal–Organic Framework: Accurate Structure and Guest Molecule Location Determined by Continuous-Rotation Electron Diffraction. *Chemistry–A European Journal* **24**, 17429-17433 (2018).

5 Kresse, G. & Furthmüller, J. Efficient iterative schemes for ab initio total-energy calculations using a plane-wave basis set. *Physical review B* **54**, 11169 (1996).

6 Perdew, J. P., Burke, K. & Ernzerhof, M. Generalized gradient approximation made simple. *Physical review letters* **77**, 3865 (1996).

7 Plimpton, S. Fast parallel algorithms for short-range molecular dynamics. *Journal of computational physics* **117**, 1-19 (1995).

8 Rappé, A. K., Casewit, C. J., Colwell, K., Goddard III, W. A. & Skiff, W. M. UFF, a full periodic table force field for molecular mechanics and molecular dynamics simulations. *Journal of the American chemical society* **114**, 10024-10035 (1992).

9 Li, Z., Turner, J., Siepmann, J. I. & Snurr, R. Q. Understanding Pore Filling Processes and Adsorption/Desorption Hysteresis in Nanoporous Metal–Organic Frameworks: Insights from Grand Canonical Monte Carlo Simulations and Free Energy Calculations. *Langmuir* (2025).

10 Potoff, J. J. & Siepmann, J. I. Vapor–liquid equilibria of mixtures containing alkanes, carbon dioxide, and nitrogen. *AIChE journal* **47**, 1676-1682 (2001).